Accumulation of non-outer segment proteins in the outer segment underlies photoreceptor degeneration in Bardet–Biedl syndrome

Poppy Datta[a], Chantal Allamargot[b], Joseph S. Hudson[a], Emily K. Andersen[a], Sajag Bhattarai[a], Arlene V. Drack[a], Val C. Sheffield[c,d], and Seongjin Seo[a,1]

[a]Department of Ophthalmology and Visual Sciences, University of Iowa College of Medicine, Iowa City, IA 52242; [b]Central Microscopy Research Facility, University of Iowa, Iowa City, IA 52242; [c]Department of Pediatrics, University of Iowa College of Medicine, Iowa City, IA 52242; and [d]Howard Hughes Medical Institute, University of Iowa College of Medicine, Iowa City, IA 52242

Edited by Jeremy Nathans, Johns Hopkins University, Baltimore, MD, and approved July 8, 2015 (received for review May 22, 2015)

Compartmentalization and polarized protein trafficking are essential for many cellular functions. The photoreceptor outer segment (OS) is a sensory compartment specialized for phototransduction, and it shares many features with primary cilia. As expected, mutations disrupting protein trafficking to cilia often disrupt protein trafficking to the OS and cause photoreceptor degeneration. Bardet–Biedl syndrome (BBS) is one of the ciliopathies associated with defective ciliary trafficking and photoreceptor degeneration. However, precise roles of BBS proteins in photoreceptor cells and the underlying mechanisms of photoreceptor degeneration in BBS are not well understood. Here, we show that accumulation of non-OS proteins in the OS underlies photoreceptor degeneration in BBS. Using a newly developed BBS mouse model [Leucine zipper transcription factor-like 1 (*Lztfl1*)/*Bbs17* mutant], isolated OSs, and quantitative proteomics, we determined 138 proteins that are enriched more than threefold in BBS mutant OS. In contrast, only eight proteins showed a more than threefold reduction. We found striking accumulation of Stx3 and Stxbp1/Munc18-1 and loss of polarized localization of Prom1 within the *Lztfl1* and *Bbs1* mutant OS. Ultrastructural analysis revealed that large vesicles are formed in the BBS OS, disrupting the lamellar structure of the OS. Our findings suggest that accumulation (and consequent sequestration) of non-OS proteins in the OS is likely the primary cause of photoreceptor degeneration in BBS. Our data also suggest that a major function of BBS proteins in photoreceptors is to transport proteins from the OS to the cell body or to prevent entry of non-OS proteins into the OS.

photoreceptor degeneration | trafficking | primary cilia | outer segment | retinitis pigmentosa

The photoreceptor outer segment (OS) is a unique modification of the primary cilium, which exists in most differentiated cells. One remarkable feature of the OS is its continuous renewal to prevent accumulation of damaged proteins caused by photooxidative stress. Older components are constantly shed at the distal end of the OS, and new proteins are delivered at the proximal end, which is linked to the cell body [the inner segment (IS)], where proteins are produced (1–3). This OS renewal is a daunting task for the trafficking system, transporting nearly 700 rhodopsin (Rho) molecules per second in frogs and 80 in mice (1, 4). The mouse rod OS is completely renewed within 10 days (2). Not surprisingly, mutations impairing protein trafficking to the OS cause various types of photoreceptor degeneration, and considerable research efforts have been made to elucidate mechanisms of protein trafficking to the OS (1, 5, 6).

In contrast, the presence and significance of active protein transport from the OS to the IS (i.e., retrograde direction) has not been clarified. Several proteins such as transducin and arrestin are known to translocate in the retrograde direction in response to changes in light conditions (7). However, these proteins mainly rely on diffusion for their translocation (8, 9). Intraflagellar transport (IFT) A complex proteins mediate retrograde trafficking in cilia (10, 11), and depletion of the retrograde IFT motor, cytoplasmic dynein-2, causes photoreceptor degeneration in zebrafish (12). However, the main role of IFT-A proteins in photoreceptors has been assumed to be to recycle "empty" IFT particles, such that they can be reused for the next round of anterograde trafficking. It is also assumed that the rapid renewal of the OS negates a need for retrograde trafficking for protein turnover.

Bardet–Biedl syndrome (BBS) is a genetically heterogeneous, autosomal recessive disease associated with ciliary dysfunction. Individuals with BBS display retinal degeneration, obesity, and polydactyly as major clinical features. Patients with BBS also frequently present with renal anomalies, diabetes, hypertension, and cognitive impairment. Among the 19 BBS genes identified thus far, eight (BBS1, BBS2, BBS4, BBS5, BBS7, BBS8, BBS9, and BBIP1) form a complex called the BBSome (13, 14). In cultured mammalian cells, *Chlamydomonas*, and *Caenorhabditis elegans*, BBSome components are found within primary cilia, predominantly enriched near the ciliary base, and pericentriolar areas (13, 15–18). Notably, the BBSome comigrates with IFT complexes within cilia (15, 16, 18), suggesting BBS proteins are involved in ciliary protein trafficking. Two models have been proposed for the molecular functions of the BBSome. First, Lechtreck et al. proposed that the BBSome functions as an adapter between IFT particles and ciliary cargos and mediates export of specific signaling proteins from cilia (15, 19). The second model, proposed by Jin et al., postulates that the BBSome functions as a coat complex to target membrane proteins to cilia (20).

Significance

The photoreceptor outer segment (OS) is a cellular compartment that senses light in the eye. Structural and functional defects in the OS are common causes of inherited blindness. Bardet–Biedl syndrome (BBS) is a human genetic disease associated with defective protein trafficking and blindness. However, it is not well understood why or how photoreceptors die in BBS. In this article, we show that the primary cause of photoreceptor degeneration in BBS is likely aberrant accumulation of non-OS proteins in the OS, which is accompanied by OS disorganization and deficiencies of certain proteins in the cell body, resulting from their sequestration in the OS. Our study provides important clues to the pathogenic mechanisms of BBS and the molecular functions of BBS proteins in vivo.

Author contributions: S.S. designed research; P.D., C.A., J.S.H., E.K.A., S.B., A.V.D., and S.S. performed research; V.C.S. contributed new reagents/analytic tools; P.D., A.V.D., and S.S. analyzed data; and S.S. wrote the paper.

The authors declare no conflict of interest.

This article is a PNAS Direct Submission.

[1]To whom correspondence should be addressed. Email: seongjin-seo@uiowa.edu.

This article contains supporting information online at www.pnas.org/lookup/suppl/doi:10.1073/pnas.1510111112/-/DCSupplemental.

However, these two models are not mutually exclusive, and the BBSome may be involved in protein transport in both directions.

Despite recent advances in our understanding of the molecular functions of the BBSome and other BBS proteins, the precise role of the BBSome and its cargos in each affected tissue is not well understood. As a consequence, pathological mechanisms of each phenotypic component of BBS, particularly photoreceptor degeneration, are poorly understood. For example, Rho was considered as a BBSome cargo, and Rho mislocalization was suggested as a potential mechanism for photoreceptor degeneration (21), on the basis of the observation that some Rho mislocalizes in old BBS animals (22), the requirement of Rab8 in Rho trafficking (23), and the interaction of the BBSome with Rabin8 [a guanine nucleotide exchange factor (GEF) for Rab8] (13). However, the vast majority of Rho localizes properly to the OS in BBS retinas, indicating that BBS proteins are not essential for Rho trafficking to the OS, and the underlying mechanisms of photoreceptor degeneration remain elusive.

LZTFL1 was initially identified as a BBSome-interacting protein that regulates ciliary localization of the BBSome (17). *LZTFL1* mutations were then found in human patients with BBS, rendering it the 17th BBS gene (*BBS17*) (24, 25). More recently, it was shown that Lztfl1 cycles between cilia and the cytoplasm and facilitates removal of the BBSome from cilia (26). In this work, we sought to determine the physiological roles of BBS proteins in photoreceptors and mechanisms of photoreceptor degeneration by using a newly developed *Lztfl1* mutant mouse line and quantitative analyses of the OS proteome.

Results

Generation of Lztfl1 Mutant Mice. The *Lztfl1* mutant mouse line was generated using an ES cell line, in which a gene trap cassette was introduced within the third intron (Fig. 1 *A* and *B*). The strong splice acceptor site at the 5′ end of the gene trap cassette is expected to intercept the upstream exons of *Lztfl1* and block their splicing to the downstream exons. To examine expression of *Lztfl1*, we collected the brain (cerebrum, cerebellum, and hypothalamus), eye, kidney, and testis and conducted immunoblotting. As shown Fig. 1*C*, Lztfl1 protein levels were below the detection limit in all tissues examined, indicating the mutated allele is either a strong hypomorph or a null.

We then examined whether *Lztfl1* mutant mice display typical BBS phenotypes. BBS mouse models described thus far commonly exhibited retinal degeneration, obesity, and ventriculomegaly (22, 27–30). Similar to other BBS mouse models, *Lztfl1* mutant animals became obese as they aged (Fig. 2*A*). By age 16–18 wk, the body weight of *Lztfl1* mutant mice was significantly heavier than that of their wild-type littermates. Magnetic resonance imaging (MRI) analysis indicated that both subcutaneous and visceral fats noticeably increased in both males and females (Fig. 2*B*). *Lztfl1* mutant animals also displayed ventriculomegaly (Fig. 2*C*). However, the severity of ventriculomegaly in *Lztfl1* mutant animals was significantly milder than that of other BBS models previously described (27, 30). Finally, we examined photoreceptor degeneration in *Lztfl1* mutants. Similar to other BBS mutant animals (22, 27–30), photoreceptors progressively degenerated in *Lztfl1* mutant retinas (Fig. 2*D*). Until postnatal day 21 (P21), the outer nuclear layer thickness in *Lztfl1* mutant retinas was largely comparable with that of wild-type, whereas the OS was moderately shorter (~60–75% of wild-type; Fig. 2*D* and Fig. S1). Photoreceptor degeneration was evident at 2 mo of age, and the vast majority of photoreceptors were lost by 6 mo of age (Fig. 2*D*). Electroretinography (ERG) analysis also showed a significant reduction in both a- and b-wave (Fig. S2). Overall, the phenotype of *Lztfl1* mutant animals was comparable to that of previously described BBS mouse models and mimics human BBS phenotypes, verifying that loss of Lztfl1 function causes BBS.

Proteomic Analysis of Lztfl1 Mutant OS. We focused our effort on the photoreceptor degeneration component of BBS and on determining proteins transported by the BBSome in photoreceptors. To this end, we decided to use OSs isolated from wild-type and *Lztfl1* mutant retinas and label-free quantitative proteomics. Before conducting a full-scale proteomic analysis, we performed a pilot experiment to determine whether there are gross changes in the *Lztfl1* OS proteome and examined localization of five relatively abundant OS proteins (Rho, Prph2/Rds, Rom1, Pde6a, and Pde6b) and three non-OS proteins [Na/K-ATPase α3/Atp1a3 (IS plasma membrane protein), Grp78/Bip/Hspa5 [endoplasmic reticulum (ER) resident protein], and Synaptophysin/Syp (synaptic vesicle protein)]. Also, to minimize secondary changes resulting from photoreceptor degeneration, we used mouse eyes at P21, when the photoreceptor differentiation is completed but degeneration is minimal. As shown in Fig. S1, none of these proteins showed notable changes in their localization in *Lztfl1* mutant retinas, suggesting there are no massive alterations in the *Lztfl1* mutant OS proteome, at least until P21.

We then isolated OSs from wild-type and *Lztfl1* mutant retinas at P20–P21, using sucrose gradient centrifugation, and conducted label-free quantitative proteomics. Although OS proteins are highly enriched (Fig. 3 and Fig. S3), it is known that a small amount of IS proteins is often included in the OS fraction prepared by this method. To avoid detecting random changes from contamination, we applied stringent filtering criteria. First, we repeated the entire experiment (from OS isolation to mass spectrometry) four times and conducted two-tailed *t* test (cutoff:

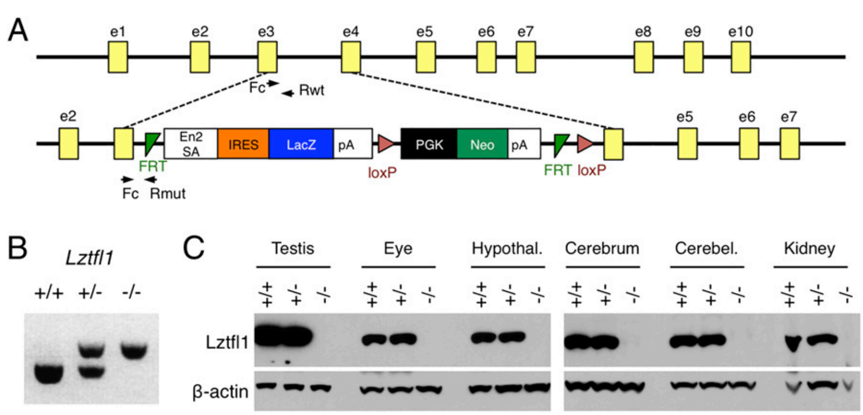

Fig. 1. Generation of *Lztfl1* mutant mice. (*A*) Schematic representation of wild-type (*Top*) and targeted (*Bottom*) *Lztfl1* alleles. (*B*) Representative PCR results of genotyping. (*C*) Western blot analysis of various tissues confirming the absence of Lztfl1 protein in mutant animals. β-actin was used as a loading control.

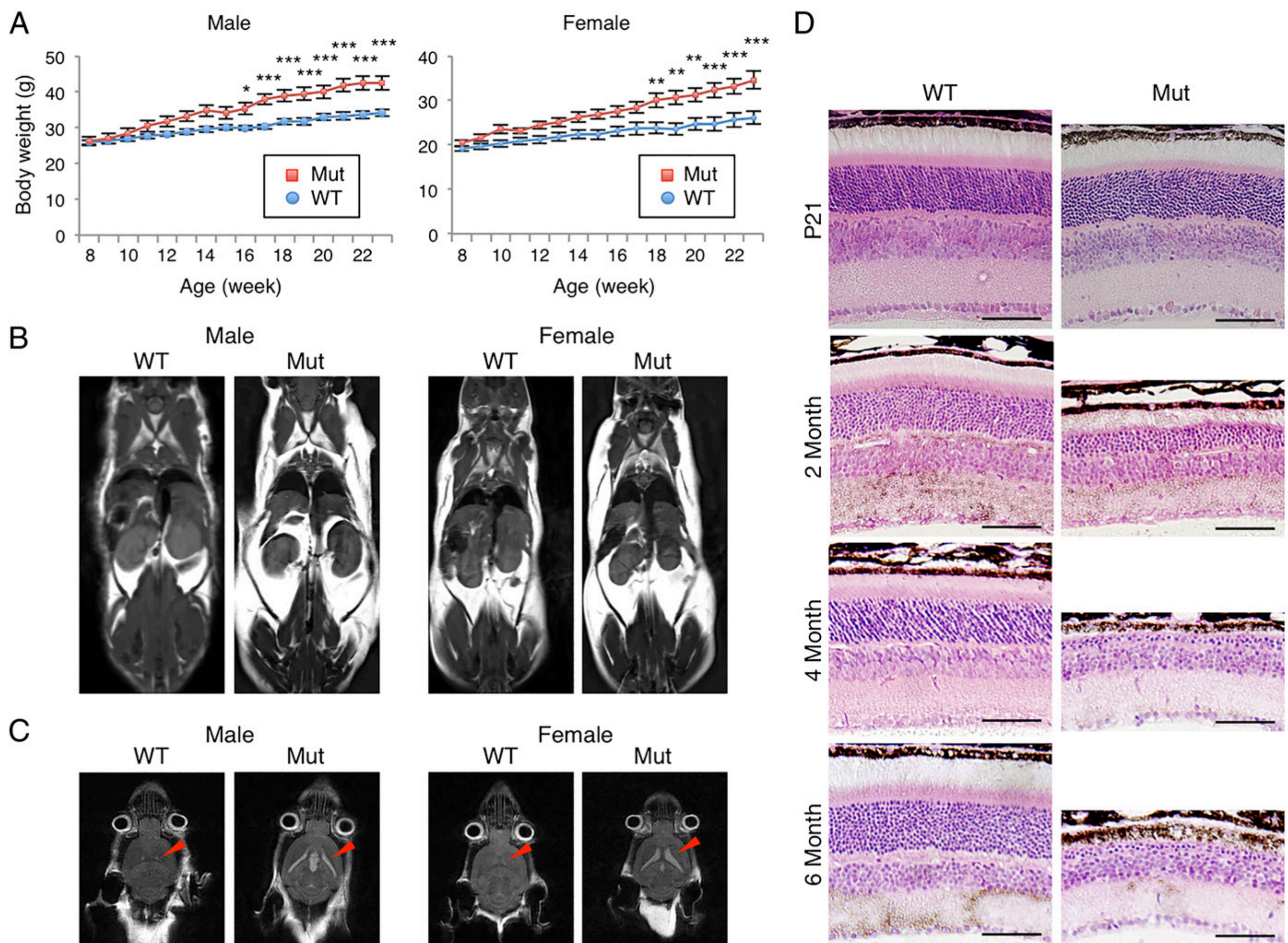

Fig. 2. Loss of *Lztfl1* function causes obesity, ventriculomegaly, and retinal degeneration in mice. (*A*) Increased body weight of *Lztfl1* mutant (Mut) mice compared with their wild-type (WT) littermates. Data are mean ± SEM; n = 9–16 animals per group. Two-way ANOVA followed by Bonferroni posttest was used for statistical analysis. *$P < 0.05$; **$P < 0.01$; ***$P < 0.001$. (*B*) MRI of body fats. Representative T1-weighted MRI images from 6-mo-old wild-type (WT) and *Lztfl1* mutant (Mut) animals are shown. White parts represent fat tissues, and gray/black areas, muscle and water. (*C*) MRI images of 6-mo-old wild-type and *Lztfl1* mutant mice showing enlarged ventricles. Red arrowheads mark the lateral ventricle. (*D*) Hematoxylin & eosin staining of wild-type and *Lztfl1* mutant retinas at the indicated ages. (Scale bar, 50 μm.)

$P < 0.05$). Then, we used average fold-change value 3 as a second cutoff to remove moderately changed proteins. This two-step filtering removed the vast majority of IS proteins, as well as obvious contaminants such as keratins, because their quantities were similar in both normal and *Lztfl1* mutant OS samples. Most OS proteins were also filtered out for the same reason. For example, Rho, Prph2, Rom1, Pde6a, and Pde6b, localization of which is not altered in *Lztfl1* mutant OSs (Fig. S1), showed only marginal changes (less than 1.5-fold reduction). After this filtering, a total of 138 proteins were determined to be enriched in *Lztfl1* mutant OS (Table 1 and Datasets S1 and S2). In contrast, only eight proteins were found reduced more than threefold. All of these proteins showed highly consistent results in all four measurements. It should also be noted that many of the enriched proteins were never detected in wild-type OS preparations, while being repeatedly detected (with similar quantities) in all four mutant samples, suggesting these proteins are unlikely to be contaminants that happen to have a similar isopycnic density as OSs.

The Database for Annotation, Visualization and Integrated Discovery analysis (31) of gene ontology terms (GOTERMs) for enriched proteins revealed that "protein/vesicle transport," "vesicle," and "nucleotide binding" are the most enriched terms in GOTERM-BP (biological process), GOTERM-CC (cellular component), and GOTERM-MF (molecular function) categories, respectively (Dataset S3). In addition, about two thirds of enriched proteins are membrane-associated proteins (i.e., transmembrane, lipid-anchored, or peripheral membrane proteins). Interestingly, four of the eight reduced proteins are cone-specific proteins, whereas the vast majority of enriched proteins are expressed in rods or in both rods and cones.

Western Blot Verification of Proteomic Changes. Next, we verified our proteomics results, using immunoblotting (Fig. 3). First, we examined levels of unchanged proteins (Rho, Prph2, Rom1, Pde6a, and Pde6b). Consistent with the modest shortening of the OS, levels of these OS proteins in individual eyes (total eye extract) were moderately reduced (45–85% of wild-type) in *Lztfl1* mutant retinas. Importantly, however, the quantity of these proteins in our OS preparations, which were normalized by total protein quantities, showed no significant differences between normal and *Lztfl1* retinas. These data suggest the quantity of these OS proteins per a unit length of the OS (or the concentration in the OS) is not significantly changed. We then turned our attention to enriched and reduced proteins and examined

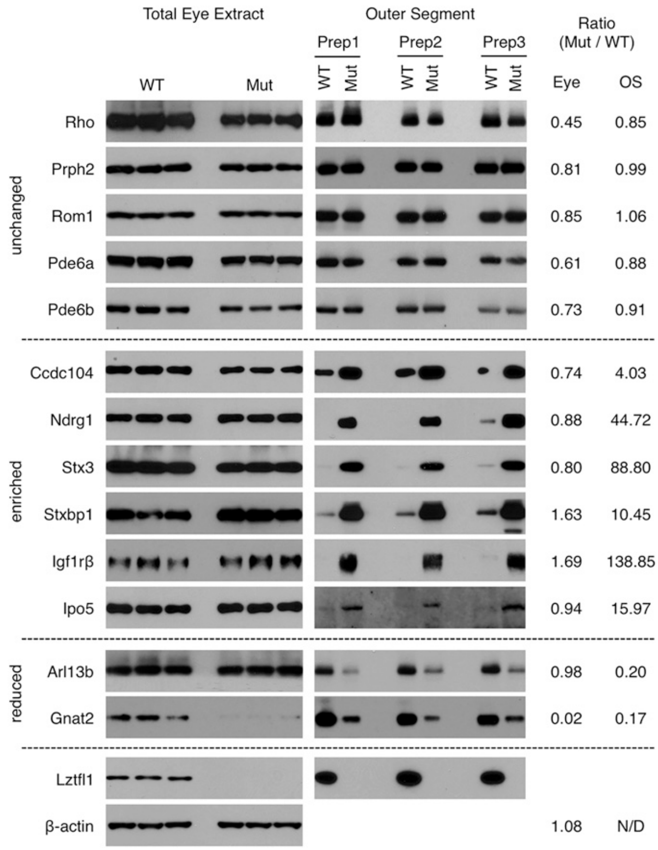

Fig. 3. Western blot analysis of enriched and reduced proteins in *Lztfl1* mutant OS. (*Left*) Each lane represents total eye extract from individual animals. Results from three animals (per genotype) are shown, and 80 μg of proteins were loaded per lane. (*Right*) Each lane represents individual OS preparations (Prep). Twenty to 25 animals were used per preparation per genotype. Shown is the result of three independent preparations, and 5 μg of proteins were loaded per lane. Note that most of the enriched proteins are undetectable or barely detectable in wild-type (WT) OS preparations. Numbers in the right are average band intensities of each protein in *Lztfl1* mutants compared with WT. Values in the column "Eye" are for total eye extract, and those of "OS" are for outer segment preparations. N/D, not detectable.

Ccdc104, Ndrg1, Stx3, Stxbp1, Igf1r (Igf1 receptor), Ipo5/RanBP5/Importin β-3, Arl13b, and Gnat2 (cone-specific transducin α subunit), for which reliable antibodies are commercially available (Fig. S4). Consistent with the proteomic data, Ccdc104, Ndrg1, Stx3, Stxbp1, Igf1r, and Ipo5 showed substantial enrichment in *Lztfl1* mutant OS fractions, whereas Arl13b and Gnat2 showed a reduction (Fig. 3). Also consistent with the proteomic data, many of the enriched proteins were undetectable or only barely detectable in wild-type OS preparations.

Accumulation of Stx3 and Stxbp1 in BBS OSs. Among the enriched proteins, Stx3 and Stxbp1 are of particular interest because they are the most abundant (based on the mass spectrometry intensity values) and are involved in membrane fusion (32). It is noteworthy that the OS is a highly membranous organelle, and the lamellar structure of the OS is disrupted by vesicles in BBS mutants (see following). Therefore, we sought to investigate their enrichment in more detail and examined their localization, using immunofluorescence microscopy. In normal photoreceptor cells, Stx3 and Stxbp1 were found mostly in the IS and the photoreceptor side of the outer plexiform layer (Fig. 4). Consistent with the previous observations (33, 34), Stx3 and Stxbp1 were found enriched near the connecting cilium, including areas

Table 1. Enriched and reduced proteins in the *Lztfl1* mutant outer segment

UniProt ID	Gene name	Fold change (KO/WT)
Q3UKC1	Tax1bp1	54.7
P43406	Itgav	51.4
Q8BKC5	Ipo5	49.3
Q9JKF6	Pvrl1	37.3
E0CY23	Hspa4l	36.5
P56399	Usp5	32.4
P51436	Drd4	32.0
Q91WP1	Pvr	30.9
Q9R0M4	Podxl	29.9
Q60751	Igf1r	29.2
Q6GQT1	A2mp	28.7
E9QM38	Slc12a2	28.2
P28656	Nap1l1	23.6
J3QP68	Gm4204	23.1
Q9CR26	Vta1	20.1
O09061	Psmb1	20.0
P97792	Cxadr	19.1
Q8VEJ9	Vps4a	18.4
Q61829	Me1	17.9
Q4JG03	Huwe1	15.8
Q3U449	Bpnt1	15.7
Q9CWD9	Jam2	15.1
Q8K1K2	Psmc5	14.8
Q705X9	Acaca	14.7
Q60738	Slc30a1	14.6
Q9D7S9	Chmp5	14.4
F6QYF8	Npepps	14.1
P10605	Ctsb	13.5
Q8BHW2	Oscp1	13.4
P19096	Fasn	13.2
Q64337	Sqstm1	12.8
Q3U454	Lrp1	12.6
Q8CHG6	mKIAA0315	11.5
Q8CHC4	Synj1	11.2
Q3U422	Ndufv3	10.9
P54823	Ddx6	10.9
Q6IS27	Pdxp	10.1
Q9DBC7	Prkar1a	9.9
A2AGJ9	Slc12a6	9.8
Q99JP7	Ggt7	9.6
Q99L75	Hspa4	9.4
Q9DCP2	Slc38a3	9.4
Q91YC8	Ddb1	9.3
Q99J08	Sec14l2	9.3
O35316	Slc6a6	8.8
Q80XH2	Impg2	8.6
Q8R5C5	Actr1b	8.2
A2APM1	Cd44	8.2
H3BJ06	Ap2b1	8.1
Q99JR9	Ccdc104	7.9
P63037	Dnaja1	7.9
Q91WA9	Abcg4	7.8
P42932	Cct8	7.7
Q0ZM32	Pcdh15	7.6
Q3TFD2	Lpcat1	7.4
Q6DIB8	Atp2b2	7.1
Q8VCV2	Ndrg3	6.9
G3UWL2	Ppp2r1a	6.9
Q68FM0	Sept5	6.7
B1AQD7	Unc119	6.6
F8WGI9	Vldlr	6.5
Q9CXI5	Manf	6.5
Q61644	Pacsin1	6.4

Table 1. Cont.

UniProt ID	Gene name	Fold change (KO/WT)
Q99KX1	Mlf2	6.3
Q8K078	Slco4a1	6.2
D3YZP5	Rab3a	6.1
O08599	Stxbp1	5.9
Q8CEB6	Akr1e1	5.9
Q9DCT1	Akr1e2	5.9
Q9D7G0	Prps1	5.8
G3UXL2	Prps1l3	5.8
Q3UUU4	Sept6	5.8
E9Q3F9	Ndrg1	5.8
E0CYE2	Impdh1	5.7
O88342	Wdr1	5.6
F7B327	Gls	5.5
Q9JK98	Clu	5.4
Q9R1P1	Psmb3	5.4
Q9CQV1	Pam16	5.4
Q9D1C8	Vps28	5.3
Q9CQ62	Decr1	5.1
F6Q609	Cct3	5.1
Q3UGE0	Sept7	5.0
F6Y9T6	Pi4ka	5.0
E9PW69	Psma4	4.9
Q05C68	Mtch2	4.9
Q3U7G3	Capza2	4.8
P61750	Arf4	4.8
Q61753	Phgdh	4.8
Q3UJV2	Capza1	4.7
Q9D9Z4	Atp6v1c1	4.7
P12382	Pfkl	4.6
P83940	Tceb1	4.6
P42125	Eci1	4.6
P80313	Cct7	4.5
Q8K3H0	Appl1	4.4
P61205	Arf3	4.3
B2RXS4	Plxnb2	4.2
Q8BSL7	Arf2	4.2
P70441	Slc9a3r1	4.2
Q8R3B4	Myof	4.2
B1AQZ0	Sept8	4.1
F6ZL13	Sh3gl2	4.0
D3Z3L2	Plekhb2	3.9
F6RN86	Abat	3.9
P84084	Arf5	3.9
Q9ESG4	Tmem27	3.9
F8SLQ4	Pex5l	3.9
Q3UE48	Tcp1	3.9
Q8R1B7	Stx3	3.9
P84078	Arf1	3.8
Q80TB8	Vat1l	3.7
Q3TMR9	Slc12a5	3.7
Q8BP17	Rab3d	3.7
P16125	Ldhb	3.7
Q9DBS2	Tprg1l	3.6
O35593	Psmd14	3.6
Q02053	Uba1	3.5
B2RUR8	Otud7b	3.5
S4R1V6	Ank2	3.5
Q9D3D9	Atp5d	3.5
Q6ZWM8	mCG_126872	3.4
Q5NDA4	Fabp7	3.4
Q3UY11	Scamp1	3.4
Q71VC6	Atp1b3	3.4
Q63915	Tf	3.3
P62137	Ppp1ca	3.3
Q9JIW9	Ralb	3.2
V6BQR3	Epb4.1l3	3.2
P21956	Mfge8	3.2
P31324	Prkar2b	3.1
Q9D6R2	Idh3a	3.1
Q8BG39	Sv2b	3.1
F6SAC3	Gm1840	3.0
D3Z0T1	Add1	3.0
Q571K0	Dlg1	3.0
Q80VP0	Tecpr1	3.0
Q71H74	Dpysl3	3.0
Q8BZW3	Glb1l2	−3.0
Q8VC33	Nxnl1	−3.3
F6QPU5	Gnat2	−4.3
B1AYN8	Opn1mw	−4.5
Q6P2B2	Csnk1g1	−4.6
Q9EQP6	Arr3	−5.2
Q6P8Y9	Gngt2	−5.5
Q640N2	Arl13b	−5.9
Q9JHQ5	Lztfl1	−38.5

between the base of the OS and the distal end of the IS, but were not detected in the rest of the OS. Additional signal was detected in the inner plexiform layer. However, in *Lztfl1* mutant retinas, both Stx3 and Stxbp1 displayed striking accumulation in the OS, whereas the pool in the remaining parts of photoreceptors was greatly reduced. Within the OS, Stx3 and Stxbp1 were found dispersed throughout the OS. Their localization in the inner plexiform layer was not affected. To examine whether other SNARE [soluble NSF (N-ethylmaleimide-sensitive fusion protein) attachment protein receptor] complex components also accumulate in the OS, we probed localization of Snap25 and Vamp2, which interact with Stx3 in the eye (Fig. S5). As shown in Fig. 4, and consistent with our proteomics data (Dataset S1), localization of Snap25 and Vamp2 was not altered in *Lztfl1* mutant retinas, indicating that accumulation of Stx3 and Stxbp1 is specific to these SNARE proteins.

Among the reduced proteins, we examined localization of Arl13b, Gnat2, and Opn1mw (Fig. 5). Consistent with our proteomics data, OS localization of these proteins was significantly reduced in *Lztfl1* mutant retinas. Instead, they showed moderate accumulation in the IS and at the synaptic terminal.

Because the BBSome shuttles between the cell body and the cilium and Lztfl1 is required for the ciliary exit phase of the recycling circle (26), loss of Lztfl1 and loss of BBSome components are expected to result in similar deficiencies in overall BBSome trafficking activity. To test this, we probed localization of Rho, Prph2, Rom1, Pde6a, Syp, Stx3, Stxbp1, Snap25, Gnat2, and Opn1mw in *Bbs1*$^{M390R/M390R}$ knock-in retinas (27). As expected, localization of these proteins in *Bbs1* mutant retinas was virtually identical to that of *Lztfl1* mutants (Fig. S6), indicating that similar molecular etiology underlies the pathogenesis of photoreceptor degeneration in other BBS models.

Ultrastructural Analysis of BBS OSs and Mislocalization of Prom1. We next examined the ultrastructure of the OS in *Lztfl1* and *Bbs1* mutant retinas, using transmission electron microscopy (Fig. 6*A* and Fig. S7). At P45, the lamellar structure of the OS is severely disrupted in both *Lztfl1* and *Bbs1* mutant retinas. Interestingly, abnormal vesicular structures were found in the OS in a subset of photoreceptors, often near the proximal end of the OS (Fig. 6*A*, red arrowheads). Many of these abnormal vesicles were too large to pass through the connecting cilium, suggesting they may be

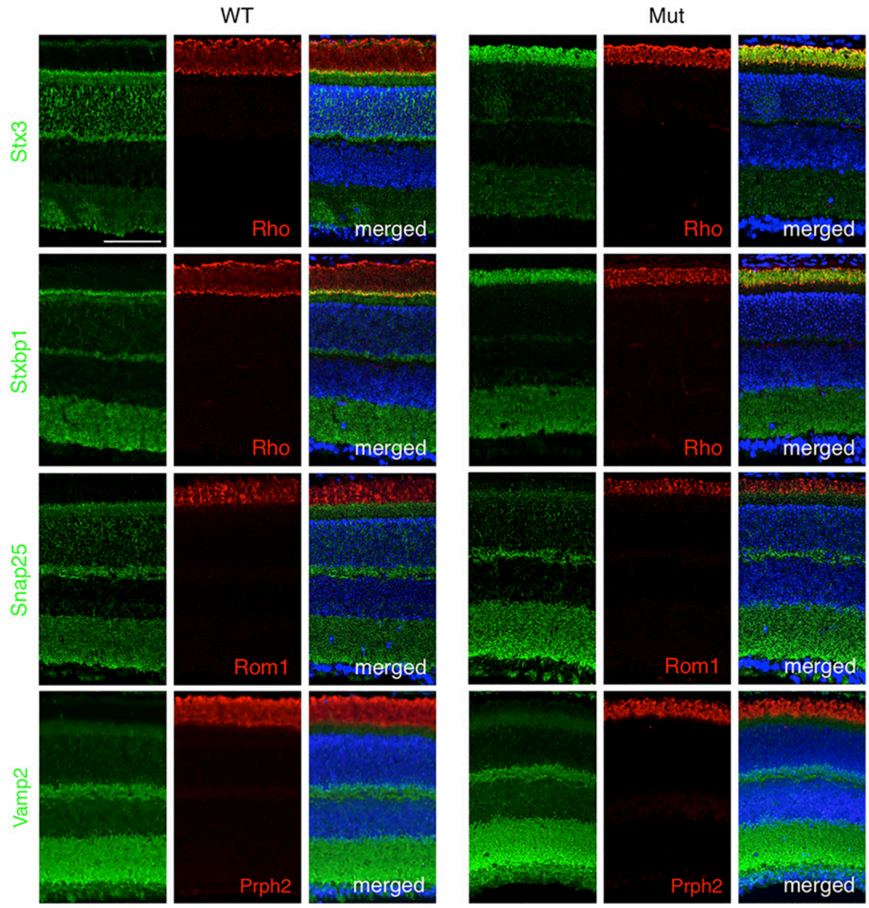

Fig. 4. Accumulation of Stx3 and Stxbp1 in the *Lztfl1* mutant OS at P21. Wild-type (WT) and *Lztfl1* mutant retinas were stained with Stx3, Stxbp1, Snap25, and Vamp2 antibodies (green). The OS was marked by Rho, Rom1, and Prhp2 antibodies (red). DAPI (blue) was used to stain nuclei, and merged images were shown in the third panels. (Scale bar, 50 μm.)

formed inside the OS, presumably by fusion of smaller vesicles. Finally, we found that discs of another subset of photoreceptors were formed along the longitudinal axis of the photoreceptor cell (Fig. 6*A*, green arrowhead). This disk morphogenesis defect is similar to what was observed in *Prom1* mutant photoreceptor cells, mutations of which cause progressive retinal degeneration in mammals (35–37). Therefore, although Prom1 showed only a moderate change in our quantitative proteomic study (~50% reduction in *Lztfl1* OSs compared with wild-type; Dataset S1), we examined localization of Prom1 in *Lztfl1* and *Bbs1* mutant retinas. Consistent with the previous studies (36, 37), Prom1 localized to the base of the OS in wild-type retinas (Fig. 6*B*). In both *Lztfl1* and *Bbs1* mutant retinas, Prom1 was still found within the OS. However, its localization was no longer limited to the OS base and was found dispersed throughout the OS. These data suggest that BBS proteins are required to limit Prom1 localization to the base of the OS.

Discussion

Our findings provide several important clues to the mechanisms of photoreceptor degeneration in BBS and the roles of BBS proteins in photoreceptors. First, our data suggest that the primary cause of photoreceptor degeneration in BBS is likely the accumulation of non-OS proteins in the OS, rather than failure of protein delivery to the OS. Our unbiased proteomic study and immuno-localization study demonstrate that a subset of IS proteins ectopically accumulate in the OS, whereas most OS proteins show no or only marginal reductions in BBS mutant retinas. Accumulation of non-OS proteins is accompanied by structural defects in the OS. Therefore, our data support the previously proposed hypothesis that BBS is a degenerative disease resulting from aberrant accumulation of proteins in cilia that leads to a progressive loss of ciliary function (15, 19). Our work further identifies specific proteins that accumulate in the BBS OS, enabling more precise understanding of the pathogenic mechanisms at the molecular level.

Accumulation of non-OS proteins in the OS may be sufficient to induce photoreceptor cell death. Accumulation of non-OS proteins is expected to interfere with or disorganize the orderly assembly of the phototransduction machinery in the disk. In addition, aberrant vesicle formation and longitudinally oriented discs were observed in BBS mutant OSs. Disorganization of the phototransduction machinery and/or structural defects in the OS may be sufficient to trigger photoreceptor cell death by yet-unknown mechanisms. Although the causal relationship between the Prom1 mislocalization and the structure defects in the BBS OS is currently unclear, Prom1 mislocalization may contribute to the retinal degeneration.

Concomitant with the accumulation of non-OS proteins in the OS is the dearth of these proteins in the cell body (i.e., IS, nucleus, or synaptic terminal), where they mainly function. Therefore, photoreceptor cell death could be a result of insufficient protein functions in the cell body. For example, in normal photoreceptor cells, Stx3 and Stxbp1 are mostly found in the IS and the synaptic terminal. In contrast, these proteins are highly enriched in the OS, and their pool in the rest of the photoreceptor is severely reduced

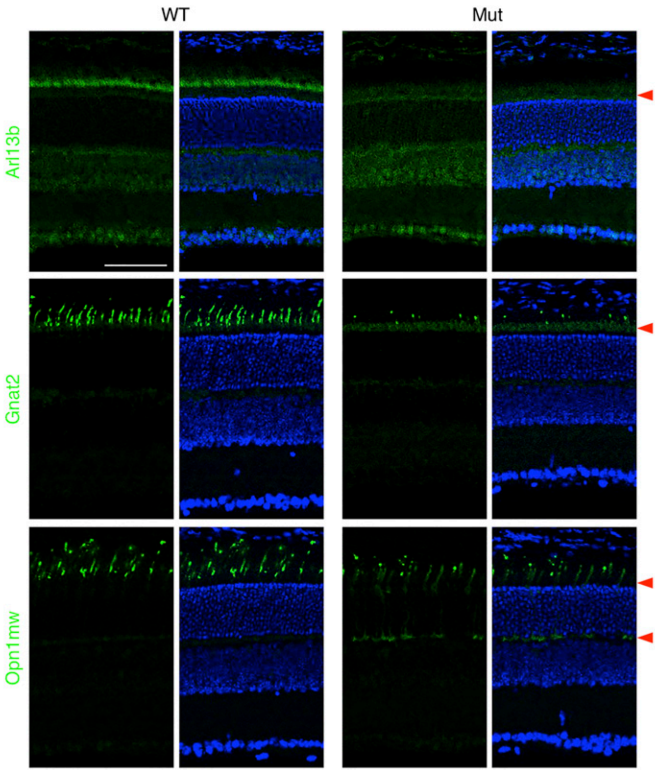

Fig. 5. Localization of Arl13b, Gnat2, and Opn1mw in *Lztfl1* mutant retinas at P21. Accumulation of Arl13b, Gnat2, and Opn1mw (green) in the IS and at the synaptic terminal of *Lztfl1* mutant retinas is marked by red arrowheads. (Scale bar, 50 μm.)

in BBS mutant photoreceptors. Stx3 and Stxbp1 are components of the SNARE complex that mediates membrane fusion events, which is the final step of vesicle trafficking. Indeed, Stx3 has been linked to Rho trafficking in photoreceptors (33, 34). An insufficient supply of Stx3 and Stxbp1 in the IS may result in a delay or failure of vesicle fusion at the IS/OS interface. Although we were not able to quantify it in our micrographs, accumulation of vesicles was observed near the base of connecting cilium of *Bbs4* mutant photoreceptors (38). This phenotype could be a result of the deficiency of Stx3 and Stxbp1 in the IS. Shortening of the OS in *Bbs1* and *Lztfl1* mutant mice and cytoplasmic dynein-2 morphant zebrafish (12) is also consistent with this notion and with overall reduction of protein delivery to the OS. In this scenario, BBS proteins are indirectly required for OS protein trafficking. Future work will determine whether accumulation or sequestration of a specific protein or proteins is sufficient to induce photoreceptor degeneration.

Second, our data suggest that a major role of the BBSome in photoreceptors is either transporting proteins from the OS to the IS (i.e., in the retrograde direction) or preventing entry of non-OS proteins into the OS. Studies in model organisms including *Chlamydomonas reinhardtii* and *C. elegans* and cultured mammalian cells have shown that the BBSome moves in and out of cilia, as well as along the ciliary axoneme together with the IFT particles (13, 15–18). In addition, several proteins have been shown to be absent or abnormally accumulating within cilia upon loss of BBS proteins (15, 39, 40). Therefore, it has been thought that the BBSome is involved in protein trafficking to and from cilia, resulting in the two models for the BBSome function described earlier (see *Introduction*). Our systemic analysis of the OS proteome suggests that, at least in rod photoreceptor cells, the main physiological role of the BBSome is likely exporting proteins from the OS, whereas the BBSome is mostly dispensable for protein import into the OS. Dispersed localization of Prom1 within the BBS OS is also consistent with the retrograde trafficking role of the BBSome.

Our data, however, do not rule out a role for the BBSome as a diffusion barrier or a gatekeeper specific to certain IS proteins. Our data suggest that the "general" diffusion barrier is intact in BBS mutant photoreceptors. For example, OS proteins Rho, Prph2, Rom1, Pde6a, and Pde6b do not show noticeable leakage to the IS before degeneration is evident. More important, IS plasma membrane proteins Atp1a3 (Na/K-ATPase α3) and Snap25 do not accumulate in BBS mutant OSs, as well as Grp78 (ER resident protein) and Synaptophysin (synaptic vesicle protein). Strong accumulation of Stx3 and Stxbp1 in the OS with a very low level in the IS (instead of more diffused or even distribution) likewise suggests that the "general" diffusion barrier is likely to be intact. However, Lztfl1 and the BBSome may be a part of a "protein-specific" diffusion barrier or a gatekeeper that prevents certain specific IS proteins from entering the OS. Live cell imaging in wild-type and BBS mutant photoreceptors will provide further insight.

One unique feature of protein trafficking in photoreceptors is that membrane proteins with no targeting signals are delivered to the OS as a default destination (41). In contrast, membrane proteins without ciliary targeting sequences do not localize to cilia in cultured mammalian cells. Therefore, accumulation of non-OS proteins in the BBS mutant OS could be unique to or more pronounced in photoreceptor cells compared with in other cell types. However, aberrant vesicular structures and bulging were observed in brain ependymal and airway epithelial cell cilia in BBS mutants (27, 42). These observations are similar to the abnormal vesicle formation in the BBS OS and suggest that similar mechanisms are likely to underlie the pathogenesis of BBS in other tissues. Finally, our data do not rule out a role of the BBSome for ciliary import. For example, several OS proteins (particularly cone-specific proteins) are significantly reduced in *Lztfl1* mutant OS and accumulate in the IS. Some of these proteins may be transported to the OS by the BBSome. It is also interesting that Rho (rod opsin) does not noticeably accumulate in the IS, but Opn1mw (cone opsin) does. At this time, it is unclear whether this difference is a result of a difference in their trafficking mechanisms or in their stability.

Methods

Antibodies Used. Antibodies used against BBS4 and Lztfl1 were described previously (13, 17). Other antibodies were purchased from the following sources: mouse monoclonal antibodies against BBS2 (SantaCruz, sc-365355), Rhodopsin (clone 1D4; Millipore, MAB5356), ATP1α3 (Abcam, ab2826,), β-actin (Sigma, A1978), SNAP25 (Abcam, ab24737), and VAMP2 (R&D, MAB5136); rat monoclonal antibody against Prom1 (EMD/Millipore, MAB4310); rabbit monoclonal antibodies against AIFM1 (Cell Signaling, 5318); and rabbit polyclonal antibodies against BBS7 (Proteintech Group, 18961), BBS9 (Sigma, HPA021289), PRPH2 (Proteintech Group, 18109), ROM1 (Proteintech Group, 21984), PDE6A (Proteintech Group, 21200), PDE6B (Proteintech Group, 22063), GRP78 (Abcam, ab21685), SYP (Cell Signaling, 5461), CCDC104 (Sigma, HPA017061), NDRG1 (Abcam, ab124689), PDI/P4HB (Sigma, P7372), STX3 (Proteintech Group, 15556), STXBP1 (Proteintech Group, 11459), IGF1Rβ (Cell Signaling, 3018), IPO5 (Abcam, ab137522), ARL13B (Proteintech Group, 17711), GNAT2 (Abcam, ab97501), and OPN1MW/LW (Chemicon, AB5405).

Generation of Lztfl1 Mutant Mice. The *Lztfl1* mutant mouse line was generated using ES cells from the Knockout Mouse Project (KOMP) repository [CSD50165; $Lztfl1^{tm1e(KOMP)Wtsi}$]. The mutant allele contains the "nonconditional" gene-trap cassette inserted between Exon3 and Exon4 of the *Lztfl1* gene. The ES cells were from the JM8 line, which originated from the inbred C57BL/6N strain, and were injected into albino (Tyr^c/Tyr^c) C57BL/6 blastocysts to generate chimeric animals. Chimeric mice were mated to 129/SvEv mice, and the colony was maintained in C57/129 mixed background. The C57BL/6N strain carries the $Crb1^{rd8}$ mutation (43), and the *rd8* mutation was eliminated by breeding. *Lztfl1* genotype was determined by PCR, using the following primers: F-common: TAA-CAT-GCC-ACT-TGG-ACA-TCA-TGG, R-WT:

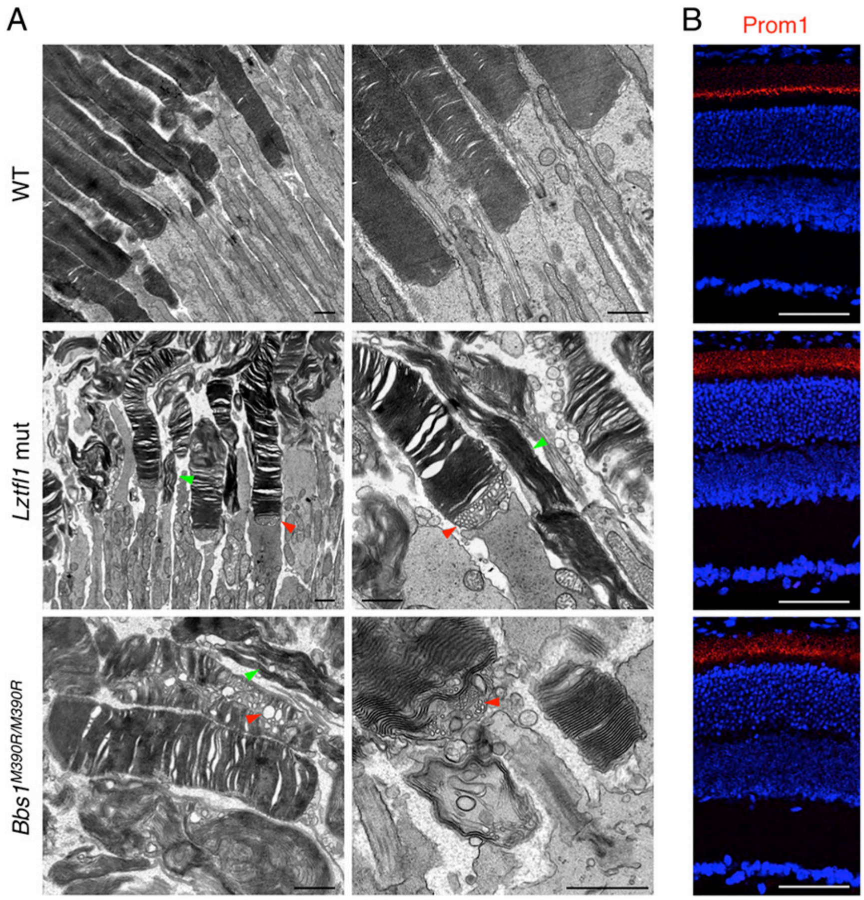

Fig. 6. Disorganization of the OS structure and Prom1 mislocalization in BBS mutant retinas. (*A*) Transmission electron micrographs from P45 wild-type (WT), *Lztfl1* mutant, and *Bbs1*$^{M390R/M390R}$ mutant retinas are shown. Sections were made to show the longitudinal axis of the photoreceptor cell. Abnormal vesicles are marked with red arrowheads and longitudinally formed discs, green arrowheads. (Scale bar, 1 μm.) (*B*) Localization of Prom1 (red) in wild-type, *Lztfl1* mutant, and *Bbs1*$^{M390R/M390R}$ mutant retinas at P21. DAPI (blue) was used to stain nuclei. (Scale bar, 50 μm.)

ATT-CCA-TGA-AAG-CTG-GTG-TTG-TGA, and R-Mut: CCA-CAA-CGG-GTT-CTT-CTG-TTA-GTC. *Bbs1* M390R knock-in mice and *rd8* genotyping were previously described (27, 43).

Histological Analysis of Mouse Eye. Mouse eyes were embedded in JB-4 resin (Electron Microscopy Sciences) following the manufacturer's instruction. Briefly, after killing animals by CO_2 asphyxiation and cervical dislocation, eyes were enucleated, and the lens and the anterior chamber were removed. The eye-cups were fixed by immersion in 4% (wt/vol) paraformaldehyde in PBS overnight. After rinsing in PBS, tissues were dehydrated in a series of increasing concentrations of ethanol/PBS [5%, 25%, 50%, 75%, and 100% (vol/vol)], followed by incubation in the Infiltration Solution [1.25% (wt/vol) benzoyl peroxide in JB-4 solution A; Electron Microscopy Science] overnight. Then tissues were placed in the embedding solution [infiltration solution with 4% (vol/vol) JB-4 Solution B] and solidified overnight at 4 °C. Five-micrometer sections were collected using a microtome (Leica Microtome, RM2135) and processed for hematoxylin and eosin staining. Photographs were taken by using an Olympus BX-41 microscope with a SPOT-RT digital camera.

ERG. ERG was conducted on 7–10-wk-old *Lztfl1* mutant mice (–/–; $n = 10$) and their wild-type littermates (+/–; $n = 8$), as described earlier (44).

MRI. Six-month-old animals (three wild-type males, three wild-type females, three *Lztfl1* mutant males, and four *Lztfl1* mutant females) were used for MRI of the brain and body fat, as previously described (27).

Isolation of Photoreceptor OS. Photoreceptor OSs were isolated by sucrose gradient ultracentrifugation following a previously described protocol (45) with some modifications. Briefly, after removing the anterior segment and the lens, the neural retina was teased away from the pigmented epithelium using forceps, collected in 63% (wt/vol) sucrose/PBS on ice, flash frozen in liquid nitrogen, and stored at −80 °C. Once sufficient numbers of retinas (∼20 wild-type and 25 *Lztfl1* mutant) were collected, retinas from each genotype were pooled in 1.5-mL tubes on ice, and the total volume was adjusted to ∼1 mL, using 63% sucrose/PBS. Then the retina suspension was gently pipetted up and down eight times, using a P1000 tip with a 1.5–2-mm orifice, and further vortexed for 20 s. The homogenate was first centrifuged at 100 × *g* for 3 min, and the supernatant was further spun at 2,200 × *g* for 10 min at 4 °C. The supernatant was transferred to an ultracentrifuge tube, and layers of 42%, 37%, and 32% sucrose/PBS solutions (1 mL each) were overlaid. The homogenate was centrifuged at 116,000 × g_{avg} for 1 h at 4 °C, using a Sorvall TH-660 rotor. OSs were collected at the 32–37% interface. The isolated OS fractions were diluted with an equal volume of ice-cold PBS and spun at 10,000 × *g* for 8 min at 4 °C. The precipitated OSs were resuspended in the OS lysis buffer (PBS with 1% Triton X-100), and protein concentrations were measured using the DC Protein Assay kit (Bio-Rad).

Label-Free Quantitative Proteomics. Fifty microgram of OS protein samples (per genotype per preparation) were submitted for label-free quantitative proteomics (Bioproximity), and total four independent sample sets were submitted. Samples were first prepared for digestion using the filter-assisted sample preparation method (46). Briefly, the protein samples were suspended in 2% (wt/vol) SDS, 50 mM Tris·HCl at pH 7.6, 3 mM DTT, sonicated shortly, and incubated in a Thermo-Mixer at 90 °C, 1,000 RPM for 20 min. After centrifugation, supernatants were buffer-exchanged to 8 M urea, 100 mM Tris·HCl at pH 7.6, and then alkylated with 15 mM iodoacetamide. The urea concentration was reduced to 2 M. Protein concentration was determined by fluorometric measurement (Qubit, Invitrogen). Samples were digested using trypsin at an enzyme-to-substrate ratio of 1:40, overnight, at 37 °C on the Thermo-Mixer at 1,000 RPM. Digested peptides were collected by centrifugation. A portion of the digested peptides, about 20 μg, were desalted using C18 stop-and-go extraction tips (47). For each sample, a C18 stop-and-go extraction tip was activated with methanol, conditioned with 60% (vol/vol) acetonitrile, 0.5% acetic acid followed by 2% acetonitrile, 0.5% acetic acid. Samples were loaded onto the tips and desalted with 0.5% acetic acid. Peptides were eluted with 60% acetonitrile, 0.5% acetic acid and lyophilized in a SpeedVac (Thermo Savant) to near dryness, approximately for 30 min. Each digestion mixture was analyzed by UHPLC-MS/MS (ultrahigh pressure liquid chromatography-mass spectrometry/mass spectrometry). LC was performed on an Easy-nLC 1000 UHPLC system (Thermo). Mobile phase A was 97.5% (vol/vol) MilliQ water, 2% acetonitrile, 0.5% acetic acid. Mobile phase B was 99.5% acetonitrile, 0.5% acetic acid. The 240-min LC gradient ran from 0% B to 35% B over the course of 210 min, and then to 80% B for the remaining 30 min. Samples were loaded directly to the column. The column was 50 cm × 75 μm i.d. and packed with 2 μm C18 media (Thermo Easy Spray PepMap). The LC was interfaced to a Quadrupole-Orbitrap mass spectrometer (Q-Exactive, Thermo Fisher) via nano-electrospray ionization, using a source with an integrated column heater (Thermo Easy Spray source). The column was heated to 50 °C. An electrospray voltage of 2.2 kV was applied. The mass spectrometer was programmed to acquire, by data-dependent acquisition, tandem mass spectra from the top 20 ions in the full scan from 400 to 1,200 *m/z*. Dynamic exclusion was set to 15 s, singly charged ions were excluded, isolation width was set to 1.0 Da, full MS resolution was set to 70,000, and MS/MS resolution was set to 17,500. Normalized collision energy was set to 25, automatic gain control to 2e5, max fill MS to 20 ms, max fill MS/MS to 60 ms, and the underfill ratio to 0.1%. Mass spectrometer RAW data files were converted to mz5 format, using msconvert (48). All searches required 5 ppm precursor mass tolerance, 0.01 Da fragment mass tolerance, strict tryptic cleavage, up to two missed cleavages, fixed modification of cysteine alkylation, variable modification of methionine oxidation, and expectation value scores of 0.01 or lower. MGF (Mascot Generic Format) files were searched using the most recent monthly update of the UniProt mouse sequence library. MGF files were searched using X!!Tandem (49), using both the native (50) and k-score (51) scoring algorithms, and by OMSSA (52). All searches were performed on Amazon Web Services-based cluster compute instances, using the Proteome Cluster interface. XML output files were parsed and nonredundant protein sets determined using Proteome Cluster (53). MS1-based peak areas were calculated using XCMS (54). Proteins were required to have one or more unique peptides across the analyzed samples with E-value scores of 0.01 or less. The raw MS2 intensity values were normalized with the total MS2 intensity. Proteins with consistent changes were determined by two-tailed t test with $P < 0.05$ as a cutoff. We used threefold change as a second cutoff to determine "significantly changed" proteins.

Immunoprecipitation and Immunoblotting. Mice were killed by CO_2 asphyxiation, followed by cervical dislocation, and tissues were collected for protein extraction. Approximately 1 mL of Lysis buffer [50 mM Hepes at pH 7.0, 150 mM NaCl, 1% Nonidet P-40, 2 mM $MgCl_2$, 2 mM EGTA, 10% (vol/vol) glycerol, protease inhibitor (Roche)] was used per 100 mg of tissue. Tissues were disrupted with a PT 1200E Polytron homogenizer (Kinematica). Lysates were centrifuged at 20,000 × g for 15 min at 4 °C. For immunoprecipitation, supernatant was incubated with indicated antibodies or normal rabbit serum for 4 h at 4 °C with rotation. Protein A/G magnetic beads (Pierce) were added and further incubated for 2 h. After washing, precipitated proteins were resuspended in 2× LDS buffer (Life Technologies). Lysates or immunoprecipitated samples were loaded on a 4–12% (wt/vol) NuPAGE gel (Life Technologies), and SDS/PAGE and immunoblotting were performed following standard protocols.

Immunofluorescence Microscopy of the Retinal Sections. Eye-cups were prepared as above and fixed in 4% (wt/vol) paraformaldehyde/PBS for 3 h at 4 °C. After washing with PBS, eye-cups were infiltrated and embedded in acrylamide as previously described (55). For Atp1a3 and Vamp2 immunostaining, eye-cups were infiltrated with 10% (vol/vol) sucrose/PBS for 2 h at room temperature and then 30% sucrose/PBS at 4 °C overnight. Eye-cups were placed in the Neg-50 embedding medium (Thermo Scientific), frozen in a dry-ice/ethanol bath, and stored at −80 °C. Fourteen-micrometer sections were obtained using a cryostat (CryoStar NX70; Thermo Scientific). Sections were processed for immunofluorescence following a standard protocol. Briefly, sections were permeabilized with PBS-T (PBS, 0.1% Triton X-100), blocked in 5% (wt/vol) BSA/5% (vol/vol) normal goat serum/PBS-T, and decorated with indicated antibodies at room temperature for 3 h or at 4 °C overnight. After rinsing, secondary antibodies conjugated to Alexa fluor 488 or 568 (Life Technologies) were bound at room temperature for 2 h. After washing, Vectashield mounting medium containing DAPI (Vector Lab) was added, and pictures were taken using Zeiss LSM 710 confocal microscope.

Transmission Electron Microscopy. After killing the mice, their eyes were enucleated and the anterior segment and the lens were removed. Eye-cups were fixed overnight at 4 °C with half-strength Karnovsky's fixative [1.5% (wt/vol) paraformaldehyde with 1.5% (wt/vol) glutaraldehyde in 0.1 M sodium cacodylate buffer (Electron Microscopy Sciences)]. After fixation, the samples were rinsed three times in 0.1 M sodium cacodylate buffer, for a total of 30 min, and treated with 1% OsO_4 (Electron Microscopy Sciences) containing 1.5% (wt/vol) potassium ferrocyanide for 1.5 h. After three additional washes in 0.1 M sodium cacodylate buffer, the eyes were rinsed in distilled water, treated with a solution of 2.5% (wt/vol) uranyl acetate (Electron Microscopy Sciences), dehydrated in graded ethanol concentrations up to 100% (vol/vol), treated with propylene oxide (Sigma), and infiltrated and embedded with Eponate 12 resin (Ted Pella) before overnight polymerization in a 70 °C oven. Next, 80-nm thick sections were cut on a Leica UC6 μLtramicrotome (Leica Microsystems Inc.), collected on copper grids, contrasted with 5% uranyl acetate and lead citrate, and examined using a Jeol 1230 transmission electron microscope (Jeol USA) equipped with a Gatan Ultrascan 2k × 2k CCD camera.

Statistics. All data were presented as mean ± SEM. Body weight data were analyzed by 2-way ANOVA, followed by the Bonferroni posttest. ERG data were analyzed by unpaired, two-tailed t test.

Study Approval. All animal studies adhered to guidelines established for the care and use of experimental animals and were approved by the Institutional Animal Care and Use Committee of the University of Iowa.

ACKNOWLEDGMENTS. We thank Daniel Thedens for conducting MRI. This work was supported by NIH Grants R01 EY022616 (to S.S.) and R01 EY011298 (to V.C.S.), Knights Templar Eye Foundation Career-Starter Research Grant (to S.S.), and Research to Prevent Blindness Special Scholar Award (to S.S.). V.C.S. is a Howard Hughes Medical Institute Investigator.

1. Pearring JN, Salinas RY, Baker SA, Arshavsky VY (2013) Protein sorting, targeting and trafficking in photoreceptor cells. *Prog Retin Eye Res* 36:24–51.
2. Young RW (1967) The renewal of photoreceptor cell outer segments. *J Cell Biol* 33(1):61–72.
3. LaVail MM (1976) Rod outer segment disk shedding in rat retina: Relationship to cyclic lighting. *Science* 194(4269):1071–1074.
4. Williams DS (2002) Transport to the photoreceptor outer segment by myosin VIIa and kinesin II. *Vision Res* 42(4):455–462.
5. Wang J, Deretic D (2014) Molecular complexes that direct rhodopsin transport to primary cilia. *Prog Retin Eye Res* 38:1–19.
6. Nachury MV, Seeley ES, Jin H (2010) Trafficking to the ciliary membrane: How to get across the periciliary diffusion barrier? *Annu Rev Cell Dev Biol* 26:59–87.
7. Sokolov M, et al. (2002) Massive light-driven translocation of transducin between the two major compartments of rod cells: A novel mechanism of light adaptation. *Neuron* 34(1):95–106.
8. Calvert PD, Strissel KJ, Schiesser WE, Pugh EN, Jr, Arshavsky VY (2006) Light-driven translocation of signaling proteins in vertebrate photoreceptors. *Trends Cell Biol* 16(11):560–568.
9. Arshavsky VY, Burns ME (2012) Photoreceptor signaling: Supporting vision across a wide range of light intensities. *J Biol Chem* 287(3):1620–1626.
10. Pedersen LB, Rosenbaum JL (2008) Intraflagellar transport (IFT) role in ciliary assembly, resorption and signalling. *Curr Top Dev Biol* 85:23–61.
11. Rosenbaum JL, Witman GB (2002) Intraflagellar transport. *Nat Rev Mol Cell Biol* 3(11): 813–825.
12. Krock BL, Mills-Henry I, Perkins BD (2009) Retrograde intraflagellar transport by cytoplasmic dynein-2 is required for outer segment extension in vertebrate photoreceptors but not arrestin translocation. *Invest Ophthalmol Vis Sci* 50(11):5463–5471.
13. Nachury MV, et al. (2007) A core complex of BBS proteins cooperates with the GTPase Rab8 to promote ciliary membrane biogenesis. *Cell* 129(6):1201–1213.
14. Loktev AV, et al. (2008) A BBSome subunit links ciliogenesis, microtubule stability, and acetylation. *Dev Cell* 15(6):854–865.
15. Lechtreck KF, et al. (2009) The Chlamydomonas reinhardtii BBSome is an IFT cargo required for export of specific signaling proteins from flagella. *J Cell Biol* 187(7):1117–1132.
16. Blacque OE, et al. (2004) Loss of C. elegans BBS-7 and BBS-8 protein function results in cilia defects and compromised intraflagellar transport. *Genes Dev* 18(13):1630–1642.
17. Seo S, et al. (2011) A novel protein LZTFL1 regulates ciliary trafficking of the BBSome and Smoothened. *PLoS Genet* 7(11):e1002358.
18. Ou G, Blacque OE, Snow JJ, Leroux MR, Scholey JM (2005) Functional coordination of intraflagellar transport motors. *Nature* 436(7050):583–587.
19. Lechtreck KF, et al. (2013) Cycling of the signaling protein phospholipase D through cilia requires the BBSome only for the export phase. *J Cell Biol* 201(2):249–261.
20. Jin H, et al. (2010) The conserved Bardet-Biedl syndrome proteins assemble a coat that traffics membrane proteins to cilia. *Cell* 141(7):1208–1219.

21. Mockel A, et al. (2011) Retinal dystrophy in Bardet-Biedl syndrome and related syndromic ciliopathies. *Prog Retin Eye Res* 30(4):258–274.
22. Nishimura DY, et al. (2004) Bbs2-null mice have neurosensory deficits, a defect in social dominance, and retinopathy associated with mislocalization of rhodopsin. *Proc Natl Acad Sci USA* 101(47):16588–16593.
23. Wang J, Morita Y, Mazelova J, Deretic D (2012) The Arf GAP ASAP1 provides a platform to regulate Arf4- and Rab11-Rab8-mediated ciliary receptor targeting. *EMBO J* 31(20):4057–4071.
24. Marion V, et al. (2012) Exome sequencing identifies mutations in LZTFL1, a BBSome and smoothened trafficking regulator, in a family with Bardet-Biedl syndrome with situs inversus and insertional polydactyly. *J Med Genet* 49(5):317–321.
25. Schaefer E, et al. (2014) Mesoaxial polydactyly is a major feature in Bardet-Biedl syndrome patients with LZTFL1 (BBS17) mutations. *Clin Genet* 85(5):476–481.
26. Eguether T, et al. (2014) IFT27 links the BBSome to IFT for maintenance of the ciliary signaling compartment. *Dev Cell* 31(3):279–290.
27. Davis RE, et al. (2007) A knockin mouse model of the Bardet-Biedl syndrome 1 M390R mutation has cilia defects, ventriculomegaly, retinopathy, and obesity. *Proc Natl Acad Sci USA* 104(49):19422–19427.
28. Mykytyn K, et al. (2004) Bardet-Biedl syndrome type 4 (BBS4)-null mice implicate Bbs4 in flagella formation but not global cilia assembly. *Proc Natl Acad Sci USA* 101(23): 8664–8669.
29. Fath MA, et al. (2005) Mkks-null mice have a phenotype resembling Bardet-Biedl syndrome. *Hum Mol Genet* 14(9):1109–1118.
30. Zhang Q, et al. (2011) Bardet-Biedl syndrome 3 (Bbs3) knockout mouse model reveals common BBS-associated phenotypes and Bbs3 unique phenotypes. *Proc Natl Acad Sci USA* 108(51):20678–20683.
31. Huang W, Sherman BT, Lempicki RA (2009) Systematic and integrative analysis of large gene lists using DAVID bioinformatics resources. *Nat Protoc* 4(1):44–57.
32. Rizo J, Südhof TC (2012) The membrane fusion enigma: SNAREs, Sec1/Munc18 proteins, and their accomplices–guilty as charged? *Annu Rev Cell Dev Biol* 28:279–308.
33. Chuang JZ, Zhao Y, Sung CH (2007) SARA-regulated vesicular targeting underlies formation of the light-sensing organelle in mammalian rods. *Cell* 130(3):535–547.
34. Mazelova J, Ransom N, Astuto-Gribble L, Wilson MC, Deretic D (2009) Syntaxin 3 and SNAP-25 pairing, regulated by omega-3 docosahexaenoic acid, controls the delivery of rhodopsin for the biogenesis of cilia-derived sensory organelles, the rod outer segments. *J Cell Sci* 122(Pt 12):2003–2013.
35. Maw MA, et al. (2000) A frameshift mutation in prominin (mouse)-like 1 causes human retinal degeneration. *Hum Mol Genet* 9(1):27–34.
36. Yang Z, et al. (2008) Mutant prominin 1 found in patients with macular degeneration disrupts photoreceptor disk morphogenesis in mice. *J Clin Invest* 118(8):2908–2916.
37. Zacchigna S, et al. (2009) Loss of the cholesterol-binding protein prominin-1/CD133 causes disk dysmorphogenesis and photoreceptor degeneration. *J Neurosci* 29(7):2297–2308.
38. Gilliam JC, et al. (2012) Three-dimensional architecture of the rod sensory cilium and its disruption in retinal neurodegeneration. *Cell* 151(5):1029–1041.
39. Loktev AV, Jackson PK (2013) Neuropeptide Y family receptors traffic via the Bardet-Biedl syndrome pathway to signal in neuronal primary cilia. *Cell Reports* 5(5):1316–1329.
40. Domire JS, et al. (2011) Dopamine receptor 1 localizes to neuronal cilia in a dynamic process that requires the Bardet-Biedl syndrome proteins. *Cell Mol Life Sci* 68(17): 2951–2960.
41. Baker SA, et al. (2008) The outer segment serves as a default destination for the trafficking of membrane proteins in photoreceptors. *J Cell Biol* 183(3):485–498.
42. Shah AS, et al. (2008) Loss of Bardet-Biedl syndrome proteins alters the morphology and function of motile cilia in airway epithelia. *Proc Natl Acad Sci USA* 105(9): 3380–3385.
43. Mattapallil MJ, et al. (2012) The Rd8 mutation of the Crb1 gene is present in vendor lines of C57BL/6N mice and embryonic stem cells, and confounds ocular induced mutant phenotypes. *Invest Ophthalmol Vis Sci* 53(6):2921–2927.
44. Seo S, et al. (2013) Subretinal gene therapy of mice with Bardet-Biedl syndrome type 1. *Invest Ophthalmol Vis Sci* 54(9):6118–6132.
45. Organisciak DT, et al. (1991) Adaptive changes in visual cell transduction protein levels: Effect of light. *Exp Eye Res* 53(6):773–779.
46. Wiśniewski JR, Zougman A, Nagaraj N, Mann M (2009) Universal sample preparation method for proteome analysis. *Nat Methods* 6(5):359–362.
47. Rappsilber J, Mann M, Ishihama Y (2007) Protocol for micro-purification, enrichment, pre-fractionation and storage of peptides for proteomics using StageTips. *Nat Protoc* 2(8):1896–1906.
48. Chambers MC, et al. (2012) A cross-platform toolkit for mass spectrometry and proteomics. *Nat Biotechnol* 30(10):918–920.
49. Bjornson RD, et al. (2008) X!!Tandem, an improved method for running X!tandem in parallel on collections of commodity computers. *J Proteome Res* 7(1):293–299.
50. Craig R, Beavis RC (2004) TANDEM: Matching proteins with tandem mass spectra. *Bioinformatics* 20(9):1466–1467.
51. MacLean B, Eng JK, Beavis RC, McIntosh M (2006) General framework for developing and evaluating database scoring algorithms using the TANDEM search engine. *Bioinformatics* 22(22):2830–2832.
52. Geer LY, et al. (2004) Open mass spectrometry search algorithm. *J Proteome Res* 3(5): 958–964.
53. Slotta DJ, McFarland MA, Markey SP (2010) MassSieve: Panning MS/MS peptide data for proteins. *Proteomics* 10(16):3035–3039.
54. Smith CA, Want EJ, O'Maille G, Abagyan R, Siuzdak G (2006) XCMS: Processing mass spectrometry data for metabolite profiling using nonlinear peak alignment, matching, and identification. *Anal Chem* 78(3):779–787.
55. Johnson LV, Blanks JC (1984) Application of acrylamide as an embedding medium in studies of lectin and antibody binding in the vertebrate retina. *Curr Eye Res* 3(7): 969–974.

CELL BIOLOGY